Journal of Solid State Chemistry 182 (2009) 2374–2384

Contents lists available at ScienceDirect

Journal of Solid State Chemistry

journal homepage: www.elsevier.com/locate/jssc

The magnetic structure of clinopyroxene-type $LiFeGe_2O_6$ and revised data on multiferroic $LiFeSi_2O_6$

Günther J. Redhammer [a,*], Georg Roth [b], Werner Treutmann [c], Markus Hoelzel [d], Werner Paulus [e], Gilles André [f], Clemens Pietzonka [g], Georg Amthauer [a]

[a] Department of Materials Engineering and Physics, Division of Mineralogy, University of Salzburg, Hellbrunnertstr. 34, A-5020 Salzburg, Austria
[b] Institute of Crystallography, RWTH Aachen University, Jägerstr. 17/19, D-52056 Aachen, Germany
[c] Institute of Mineralogy, Philipps-University Marburg, Hans Meerweinstr., D-35032 Marburg/Lahn, Germany
[d] Institute for Materials Science, Darmstadt University of Technology, Petersenstrasse 23, 64287 Darmstadt c/o FRM II, Lichtenbergstrasse 1, 85747 Garching, Germany
[e] Sciences Chimiques de Rennes - UMR 6226, Matériaux Inorganiques: Chimie Douce et Réactivité, Université de Rennes 1, Campus de Beaulieu, Bât 10B, F-35042 Rennes, France
[f] Laboratoire Léon Brillouin (UMR12 CEA-CNRS), CEA-Saclay, F-91191 Gif-Sur-Yvette Cedex, France
[g] Department of Chemistry, Philipps-University Marburg, Hans Meerweinstr., D-35032 Marburg/Lahn, Germany

ARTICLE INFO

Article history:
Received 19 March 2009
Received in revised form
1 June 2009
Accepted 8 June 2009
Available online 12 June 2009

Keywords:
Clinopyroxene
$LiFeSi_2O_6$
$LiFeGe_2O_6$
Magnetic structure
Neutron diffraction
SQUID magnetometry
Crystal structure

ABSTRACT

The clinopyroxene compounds $LiFeSi_2O_6$ and $LiFeGe_2O_6$ have been investigated by constant wavelength neutron diffraction at low temperatures and by bulk magnetic measurements. Both compounds are monoclinic, space group $P2_1/c$ and do not exhibit a change in nuclear symmetry down to 1.4 and 5 K respective. However, they transform to a magnetically ordered state below 20 K. $LiFeSi_2O_6$ shows a simple magnetic structure with no indication of an incommensurate modulation. The magnetic space group is $P2_1/c'$ and the structure is described by a ferromagnetic coupling of spins within the infinite $M1$ chains of edge-sharing octahedra, while the coupling between these $M1$ chains is antiferromagnetic. The magnetic phase transition is accompanied by magnetostriction of the lattice when passing through the magnetic phase transition. The magnetic structure of $LiFeGe_2O_6$ is different to the silicate: the space group is $P2_1'/c$ and the magnetic unit cell doubled along the a-direction. Within the $M1$ chains spins are coupled antiferromagnetically, while the chain to chain coupling is antiferromagnetic when coupling goes via the GeB tetrahedron and ferromagnetic when it goes via the GeA tetrahedron.

1. Introduction

The class of pyroxenes, general formula ABX_2O_6, is an important group of minerals which have been well studied in geosciences for decades [1–3]. As their structure accepts a wide variety of cations with $A = Na^+$, Li^+, Ca^{2+} and Sr^{2+}, B = divalent and trivalent cations including Mg, Ni, Co, Fe, Mn, Al, Ga, Sc, In, Ti^{3+}, V^{3+},… and $X = Si^{4+}$, Ge^{4+} they are ideal candidates for comparative crystal chemistry in p-T-x space. Pyroxenes adopt orthorhombic as well as monoclinic symmetries and show a variety of phase transitions as a function of temperature and pressure. Especially the Li-containing clinopyroxenes exhibit changes in symmetry from a low temperature $P2_1/c$ to a high temperature HT-$C2/c$ structure [4–5], while the HT-$C2/c$ structure transforms to $P2_1/c$ and to a high pressure HP-$C2/c$ structure when pressurized [6–8]. The clinopyroxenes however have also attracted significant interest in recent day in solid state physics due to their (low dimensional magnetic) properties at low temperatures: Ti-based pyroxenes (Na, Li)$Ti^{3+}Si_2O_6$ adopt a spin singlet ground state at about 190 K due to orbital ordering [9,10], V^{3+} based pyroxenes exhibit well developed low-dimensional behaviour, but finally reach long-range magnetic ordering at very low temperatures due to the presence of inter-chain interaction [11–15]. It is this interplay between competing intra-chain and inter-chain interaction which finally determines the type of magnetic ordering, either ferromagnetic (FM) or antiferromagnetic (AFM) in the pyroxenes. These interactions however depend critically on the geometric topologies of the atomic structure. For example in Cr-based clinopyroxenes, the overall magnetic ordering from bulk measurements appears to be antiferromagnetic in $LiCrSi_2O_6$, while it is ferromagnetic in $NaCrGe_2O_6$ [16–18]. Even if the magnetic ion does not change, the dominating magnetic properties do, caused by distinctly altered structural topologies (e.g. increasing Cr–Cr distances within and between the chains), as reviewed recently by Redhammer et al. in the course of the determination of the crystal structures of $NaCrGe_2O_6$ and $LiCrGe_2O_6$ [19].

Jodlauk et al. [20] suggested that pyroxenes constitute a new class of multiferroics. They provided evidence for magnetically driven ferroelectricity in $NaFeSi_2O_6$, $LiFeSi_2O_6$ and $LiCrSi_2O_6$. Jodlauk et al. also discussed the possibility of a spiral

* Corresponding author. Fax: +43 662 8044 622.
E-mail address: Guenther.redhammer@sbg.ac.at (G.J. Redhammer).

0022-4596/$ - see front matter © 2009 Elsevier Inc. All rights reserved.
doi:10.1016/j.jssc.2009.06.013

(incommensurate) magnetic structure, caused by magnetic frustration, to be the reason for the multiferroic behaviour. However, they stated that in the absence of reliable data on the magnetic structures of the clinopyroxenes they cannot identify the source of multiferroic behaviour [20]. The magnetic structure of $LiFeSi_2O_6$ was first evaluated by Redhammer et al. [4] and is described to have an antiferromagnetic arrangement of spins within and between the octahedral $M1$ chains. No data are available for the analogous germanate clinopyroxene-type compound $LiFeGe_2O_6$. As part of our ongoing research of the magnetic properties in the pyroxenes, we have recently studied the spin structures of $CaM^{2+}(Si,Ge)_2O_6$, $M = Fe^{2+}$, Co^{2+}, Ni^{2+} and Mn^{2+} [21]. In this present contribution we give a detailed re-evaluation of the magnetic spin structure of the multiferroic material $LiFeSi_2O_6$ and compare the data with the newly determined structure of the analogue germanate $LiFeGe_2O_6$. As stated above, the detailed knowledge of the spin arrangements in the magnetically ordered state may help to better understand multiferroic behaviour in the pyroxenes.

2. Experimental

2.1. Material synthesis

Polycrystalline sample materials of $LiFeSi_2O_6$, and $LiFeGe_2O_6$ were prepared by a solid-state ceramic sintering route in batches of ~10 g. In a first step, mixtures of Li_2CO_3, Fe_2O_3 and SiO_2/GeO_2 in the exact stoichiometry of the desired compounds were ground under ethanol, pressed to pellets, put into open platinum crucibles and fired under ambient pressure and oxygen fugacity at a temperature of 1173 K. After a sintering time of 5 days, the sample materials were reground, pressed and reheated at 1223 K for the silicate and 1273 K for the germanate. This procedure was repeated 5 times. Single-phase polycrystalline powders of the above mentioned compositions were obtained, which were pale yellow–green for the silicate and pale brown for the germanate. The single phase nature of the samples was checked by powder X-ray diffraction and inspection of the samples under the optical microscope. No impurity was detected.

2.2. SQUID magnetometry

The magnetic measurements were performed at the Philipps-University of Marburg/Lahn on a MPMS-2 SQUID magnetometer (Quantum Design, San Diego, USA). Small amounts of sample material (between 30 and 40 mg) were put into KLF containers and brought into measuring position using a straw. The variation of the magnetization as a function of temperature at fixed external magnetic field and as a function of the external field at fixed temperature was studied. A correction for the diamagnetism of the sample and the sample container was applied before calculating the susceptibilities from the magnetization data.

2.3. Neutron diffraction

Neutron powder diffraction experiments on $LiFeSi_2O_6$ were performed at the ORPHEE-reactor (Laboratoire Leon Brillouin, France) using the G4.1 diffractometer ($\lambda = 2.4249$ Å) in a temperature range between 1.4 and 52 K, 2θ range of $8^\circ \le 2\theta \le 88^\circ$, step width 0.1°. Diffraction data on $LiFeGe_2O_6$ were collected at the FRM-2 reactor (Forschungsneutronenquelle Heinz Maier-Leibnitz; Germany) using the SPODI diffractometer with Ge-331 monochromatized neutron radiation ($\lambda = 2.537$ Å). Experiments were done in a temperature range between 5 and 30 K; the 2θ range was $3^\circ \le 2\theta \le 145^\circ$, step width 0.04°. Rietveld refinements of the powder patterns were performed with FULLPROF [22]. The pseudo-Voigt function was chosen to simulate the peak-shape and the angular dependence of the FWHM was modelled with three parameters U, V and W using the formula of Cagliotti et al. [23]. Initial structural parameters were taken from 100 K single-crystal X-ray structures of the corresponding compounds of this study. Possible magnetic structures below T_N were tested using representational analysis. Due to the limited resolution in 2θ of the high intensity G4.1 diffractometer and to reduce the amount of refined parameters the U, V and W values were fixed to the resolution function of the diffractometer ($U = 0.821$, $V = -0.237$, $W = 0.078$) and only the shape parameter was refined. Also the isotropic displacement parameters of all oxygen atoms were restrained to have the same values; the same restrain was applied to the cations. As the zero-shift parameter showed a non-linear variation at the magnetic phase transition in an initial refinement series, it was fixed to a value constant at all temperatures to avoid false lattice parameters variation. No such parameter constraints were necessary for $LiFeGe_2O_6$, zero-shift and profile parameters remained constant within the entire temperature range.

3. Results and discussion

3.1. $LiFeSi_2O_6$

The magnetic structure of $LiFeSi_2O_6$ was first determined from powder neutron diffraction data by Redhammer et al. [4]. Here we present additional data of bulk magnetic measurements and a re-evaluation of our previous neutron diffraction data using irreducible representations of possible magnetic structures.

3.1.1. Bulk magnetic properties

At an external field $H = 10$ kG the magnetic susceptibility χ_{molar} of synthetic $LiFeSi_2O_6$ exhibits a sharp maximum at 20.4(2) K in its temperature dependence with the point of inflection being located at 18.4(2) K (Fig. 1A). The inverse magnetic susceptibility $1/\chi_{molar}$ (inset of Fig. 1A) shows Curie–Weiss behaviour above ~60 K. By fitting a linear regression line to the data, the paramagnetic Curie-temperature Θ_P was found to be −25.4(5) K, the experimental magnetic moment $\mu_{CW} = 5.78(5)\,\mu_B$ is close to the theoretical spin only value of $Fe^{3+} = 5.92\,\mu_B$ [24]. The negative paramagnetic Curie-temperature suggests dominating antiferromagnetic coupling in $LiFeSi_2O_6$. These findings are in good agreement with literature data by Baum et al. [25] who determined a magnetic ordering temperature of 19.5 K and a Θ_P of −33 K from magnetization measurement on a single-crystal. Measurements of χ_{molar} at different external fields H reveal a small temperature dependence of T_N. The point of inflection shifts from 21 K at $H = 1$ kG to 23.7 K at $H = 50$ kG.

The field dependence of the magnetisation $M = f(H)$ at 4 K is linear up to a field of ~25 kG, at higher fields a sluggish deviation towards higher susceptibilities is observed. To clarify this high field susceptibility measurements were performed for us by Dr. H. Ehrenberg on a 150 mg batch of $LiFeSi_2O_6$ up to high fields of 120 kG at the "Interdisciplinary Research Centre in Superconductivity" Cambridge, England, at temperatures of 4, 8, 16 and 24 K; results are shown in Fig. 1B. The sluggish S-curvature of the field dependent magnetisation is interpreted as a spin-flop transition taking place at fields of ~64.5(3)–68.5(3) kG, depending on temperature. From the available data a T–H phase diagram is constructed, which is given in the inset of Fig. 1B.

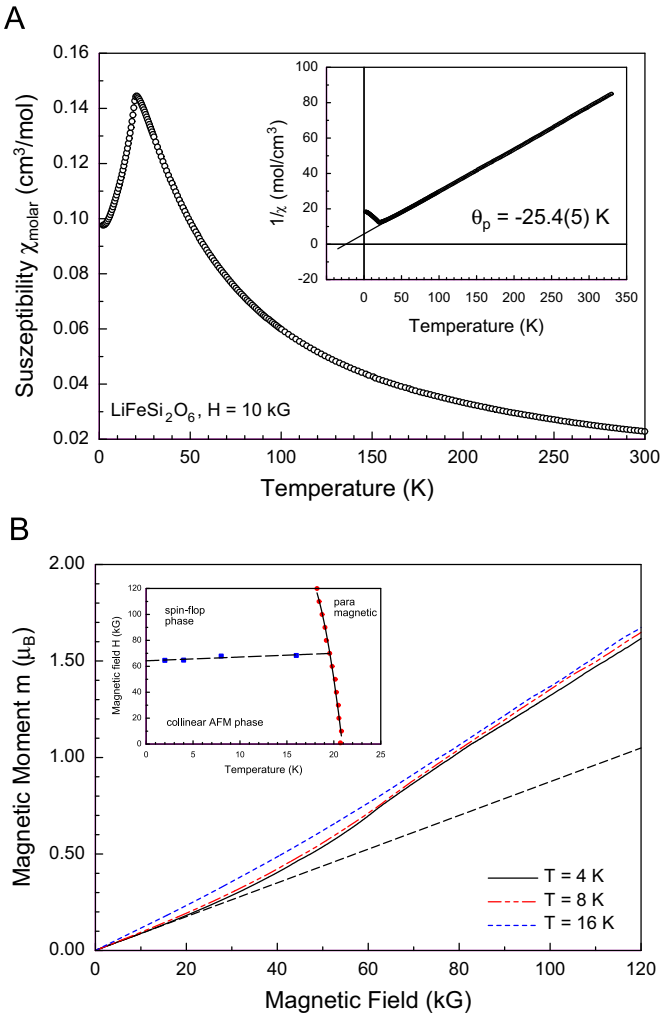

Fig. 1. (A) Magnetic susceptibility of synthetic $LiFeSi_2O_6$ at an external field of $H = 10$ kG. The inset shows the inverse magnetic susceptibility, the line fitted to the data corresponds to a Curie–Weiss law; (B) field dependence of $LiFeSi_2O_6$ at different temperatures. The long-dashed line is a linear regression line fitted to the low field data to highlight the upward deviation the magnetisation at low temperatures. The inset shows a T–H phase diagram, determined from the available data of this study (high field data courtesy of H. Ehrenberg).

3.1.2. Neutron diffraction

For $LiFeSi_2O_6$ neutron diffraction patterns were recorded between 1.4 and 52 K. The refinement of the atomic structure was done starting with the $P2_1/c$ structure of $LiFeSi_2O_6$ at 100 K as given in Redhammer et al. [4]. From the neutron diffraction data no evidence for a change in symmetry between 1.4 and 52 K is evident, i.e. the space group retains $P2_1/c$ symmetry down to the lowest temperature. Experimental details and fitting parameters for selected temperatures are compiled in Table 1 and selected structural parameters are given in Table 2.[1] Generally the $P2_1/c$ structure of $LiFeSi_2O_6$ contains an infinite zig–zag chain of edge-sharing octahedral $M1$ sites hosting the Fe^{3+} cations. These quasi one-dimensional chains are connected to each other via infinite chains of corner sharing SiO_4 tetrahedra, running parallel to the crystallographic c-axis. In contrast to the HT-$C2/c$ structure, the $P2_1/c$ structure has two distinct tetrahedral chains, which can be distinguished on basis of their O3–O3–O3 tetrahedral bridging angles: The A-chain is S-rotated with a kinking angle of 192.55(7)°, while the B-chain has an O-rotational sense with O3B–O3B–O3B is 160.02(7)° at 100 K [4], i.e. the B-chain is more kinked as compared to the A-chain. In the HT-$C2/c$ phase, these two chains become equal and almost stretched with an O3–O3–O3 angle of 180.73(7)° at 298 K [4].

The evolution of lattice parameters as a function of temperature is displayed in Fig. 2. There are some discontinuities in the metric parameters below $T<20$ K. In particular b and c show a marked decrease by ~0.045% associated with the magnetic phase transition, while β is smaller by 0.025% in the magnetically ordered state.

3.1.2.1. Magnetic structure determination. Antiferromagnetic ordering leads to the appearance of additional Bragg reflections in the neutron powder pattern. In the case of $LiFeSi_2O_6$, first additional magnetic reflections appear in the powder pattern at temperatures between 17.5 and 18.4 K. A distinct increase of the background around ~16° 2θ is evident a few degrees above the phase transition, indicative of magnetic pre-ordering phenomena. As expected for Fe^{3+} as a $3d^5$ system the magnetic Bragg reflections are strong in intensity and the (100) and (010) reflections are the strongest of all observed Bragg-peaks at low temperatures (Fig. 3). The general appearance of the diffraction pattern is similar to the ones of $CaFeSi_2O_6$ or $CaMGe_2O_6$ (M = Ni, Co) recently described in [21]. The magnetic reflections can be indexed using the same unit cell as for the atomic reflections, i.e. the propagation vector $\boldsymbol{k} = 0$. The intensity $I_{hkl}(T)$ of the two prominent magnetic reflections (100) and (010) can be fitted with a phenomenological power law [21,24,26] giving critical exponents $\beta = 0.41(2)$ and 0.40(3) for the (100) and the (010) Bragg reflection, respectively, with $T_N = 17.8(1)$ K. This is in accordance with a three-dimensional model for magnetic ordering in $LiFeSi_2O_6$.

The possible magnetic structures, compatible with the $P2_1/c$ symmetry of $LiFeSi_2O_6$ at low temperatures were determined by representational analysis, following the formalism of Bertaut [27,28] as implemented in the programme BasiReps [29]. The representation Γ is constructed with the Fourier components m^k corresponding to the Fe-atoms at the 4e position (Table 3). The decomposition of Γ in terms of the irreducible representation Γ_k for the 4e site is given as:

$$\Gamma(4e) = 3\Gamma_1 + 3\Gamma_2 + 3\Gamma_3 + 3\Gamma_4$$

The different basis vectors, which are associated with each irreducible representation were calculated with the programme BasiReps [29] using the projection operator technique. Table 4 gives the four possible magnetic structures, consistent with the $P2_1/c$ symmetry and the resulting magnetic space groups, as determined from the "magnetic space group tables" [30]. According to the refinements of the 1.4 K data, the magnetic structure is given by the irreducible representation Γ_1 with basis functions: [A_x, C_y, A_z], while all other models clearly failed to fit the experimental data. The symbols A(+ − − +) and C(+ + − −) correspond to the Bertaut's notation [27]. Using the + and − sequence of Γ_1, the refinements yield a magnetic structure with the moments oriented in the a–c plane, the component of the magnetic moment along the crystallographic b-axis is negligibly small (Table 5); several starting models with components also along b were tested, refinements however always converged to the values given in Table 5. From our data it is concluded that $LiFeSi_2O_6$ possesses a collinear magnetic structure. Within the a–c plane the magnetic moment vector is not perfectly aligned along the crystallographic c-axis but tilted away from it by ~5.8(6)°.

Below 6 K the magnetic moment shows saturation. Fitting a phenomenological power law to the data as given in Blundell et al.

[1] Atomic coordinates are available from the crystallographic information files (CIFs), which are deposited.

Table 1
Experimental details and results of Rietveld refinements on constant wavelength neutron diffraction pattern for synthetic $LiFeSi_2O_6$ and $LiFeGe_2O_6$ at some selected temperatures.

Sample	$LiFeSi_2O_6$			$LiFeGe_2O_6$		
Instrument	G4.1 (LLB)			SPODI (FRM-2)		
Wavelength (Å)	2.4249			2.5370		
Sample colour	Light green			Beige-brown		
T (K)	1.4	23.2	51	5	20	30
a (Å)	9.6515(5)	9.6510(6)	9.6513(5)	9.8662(3)	9.8674(4)	9.8679(3)
b (Å)	8.7017(5)	8.7057(7)	8.7060(6)	8.8104(4)	8.8091(4)	8.8086(4)
c (Å)	5.2766(3)	5.2790(4)	5.2792(3)	5.3714(2)	5.3705(3)	5.3701(2)
β (°)	109.899(4)	109.929(4)	109.937(4)	108.894(3)	108.877(3)	108.869(3)
V (Å^3)	416.70(4)	416.97(5)	416.99(4)	441.76(3)	441.71(3)	441.69(3)
$2\theta_{min}$ (°)	8.0	8.0	8.0	2.5	2.5	2.5
$2\theta_{max}$ (°)	87.9	87.9	87.9	153.96	153.96	153.96
Increment (°)	0.1	0.1	0.1	0.04	0.04	0.04
R_p (%)	4.32	4.11	3.45	3.48	3.80	3.60
R_{wp} (%)	5.59	5.20	4.55	4.65	5.04	4.78
R_{exp} (%)	0.68	2.05	1.32	1.60	1.61	1.59
R_B (%)	1.86	2.59	1.81	3.36	3.68	3.68
$R_{B\ magn.}$ (%)	4.35	–	–	10.0	–	–

For all data; monoclinic cell setting, space group $P2_1/c$, $Z = 4$; step scan data, refinement on F^2, pseudo-Voigt function, no excluded regions.

Table 2
Selected bond lengths (Å) and—angles (°) at some representative temperatures for synthetic $LiFeSi_2O_6$ and $LiFeGe_2O_6$ as extracted from Rietveld refinements of the neutron diffraction data.

Sample	$LiFeSi_2O_6$			$LiFeGe_2O_6$		
T (K)	1.4	23.2	51.0	5	20	30
Fe–O2*A*	1.914(16)	1.917(15)	1.893(12)	1.885(3)	1.886(3)	1.882(3)
Fe–O2*B*	1.938(16)	1.925(16)	1.949(12)	1.934(3)	1.937(3)	1.936(3)
Fe–O1*B*	1.970(12)	2.005(11)	2.007(9)	2.046(3)	2.044(3)	2.045(3)
Fe–O1*A*	2.094(16)	2.061(11)	2.060(10)	2.025(2)	2.026(3)	2.025(3)
Fe–O1*A*	2.121(12)	2.122(16)	2.124(13)	2.125(3)	2.125(3)	2.126(3)
Fe–O1*B*	2.196(17)	2.151(17)	2.156(13)	2.140(3)	2.136(3)	2.137(3)
⟨Fe–O⟩ Å	2.039	2.030	2.031	2.026	2.026	2.025
$[Fe–Fe]_{inter}$	3.173(12)	3.178(12)	3.179(10)	3.217(2)	3.215(2)	3.214(2)
$[Fe–Fe]_{intra.A}$	5.357(13)	5.285(15)	5.269(8)	5.420(2)	5.423(2)	5.424(2)
$[Fe–Fe]_{intra.B}$	5.280(13)	5.345(15)	5.361(8)	5.544(2)	5.546(2)	5.546(2)
Fe–O1*A*–Fe	97.7(5)	98.2(5)	98.9(5)	101.6(2)	101.5(2)	101.5(2)
Fe–O1*B*–Fe	99.1(5)	99.7(5)	99.5(5)	100.4(2)	100.5(2)	100.5(2)
Li–O2*B*	1.96(3)	2.02(3)	1.98(3)	2.028(7)	2.051(9)	2.037(8)
Li–O1*A*	2.01(3)	2.03(3)	2.03(3)	2.086(7)	2.090(9)	2.081(9)
Li–O1*B*	2.07(3)	2.04(3)	2.06(3)	2.107(7)	2.103(9)	2.116(9)
Li–O2*A*	2.33(3)	2.29(3)	2.32(3)	2.348(7)	2.323(8)	2.342(8)
Li–O3*A*	2.53(3)	2.53(3)	2.53(3)	2.207(6)	2.191(7)	2.194(7)
Li–O3*B*	2.72(3)	2.75(3)	2.75(2)	2.461(8)	2.452(10)	2.456(9)
⟨Li–O⟩	2.269	2.275	2.276	2.206	2.202	2.205
Si*A*–O1*A*	1.625(20)	1.727(17)	1.692(15)	1.755(3)	1.751(3)	1.755(3)
Si*A*–O2*A*	1.614(22)	1.550(20)	1.557(18)	1.730(3)	1.732(3)	1.735(3)
Si*A*–O3*A*	1.611(22)	1.561(18)	1.576(19)	1.750(3)	1.751(3)	1.749(3)
Si*A*–O3*A*	1.624(24)	1.654(21)	1.657(20)	1.755(3)	1.754(3)	1.755(3)
⟨Si*A*–O⟩	1.619	1.623	1.621	1.747	1.747	1.74(9)
$[O3–O3–O3]_A$	192.1(5)	189.8(5)	190.3(5)	209.7(2)	209.8(2)	209.6(2)
Si*B*–O1*B*	1.634(23)	1.564(17)	1.602(17)	1.757(3)	1.763(3)	1.760(3)
Si*B*–O2*B*	1.572(18)	1.653(18)	1.637(16)	1.718(3)	1.714(3)	1.713(3)
Si*B*–O3*B*	1.644(18)	1.642(20)	1.630(18)	1.763(3)	1.765(3)	1.765(3)
Si*B*–O3*B*	1.670(26)	1.698(17)	1.637(15)	1.773(3)	1.773(3)	1.773(3)
⟨Si*B*–O⟩	1.630	1.639	1.627	1.753	1.754	1.753
$[O3–O3–O3]_B$	165.4(5)	161.5(5)	160.9(5)	136.8(2)	136.7(2)	136.6(2)

[31] results in $T_N = 18.1(2)$ K with a critical exponent $\beta = 0.42(3)$. The total magnetic moment in $LiFeSi_2O_6$ at 1.4 K amounts 4.85 μ_B, which is distinctly lower than the theoretical spin only value of high spin Fe^{3+} of 5.92 μ_B [24] and also significantly lower than the (paramagnetic) moment derived from susceptibility measurements. This reduction of about 18% from the theoretical value may result from frustrations effects. The magnetic structure model is valid in the whole magnetic phase temperature range and the spin orientation remains constant (with variations between 5.8(6)° and 6.8(9)°).

The obtained magnetic structure of $LiFeSi_2O_6$ (Fig. 4) is characterized with a ferromagnetic coupling of the moments within the chains of $M1$ sites, while the chain to chain

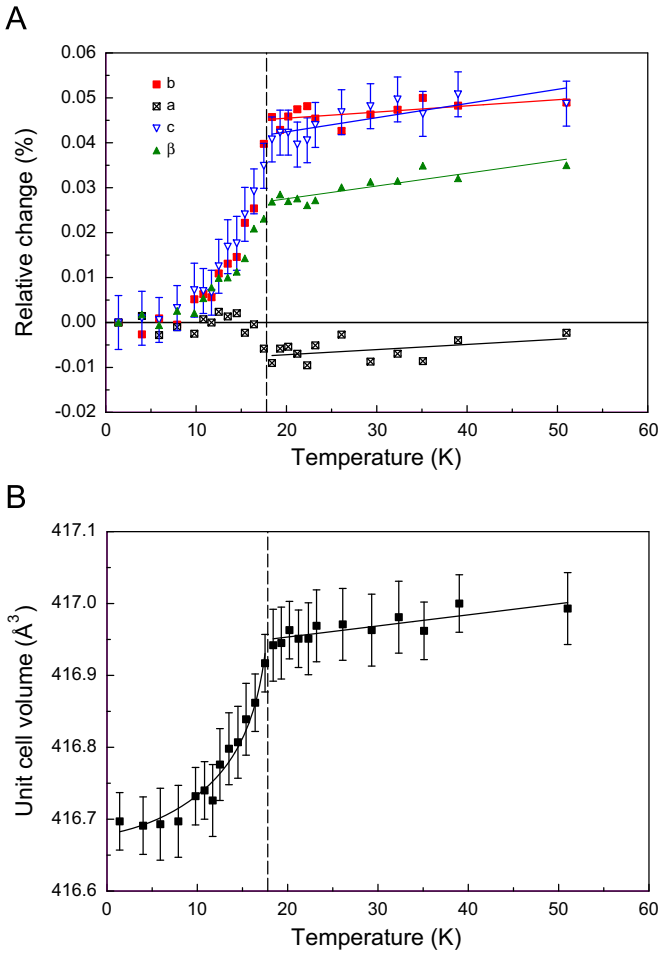

Fig. 2. (A) Changes in unit cell parameters of $LiFeSi_2O_6$ relative to the values at 1.4 K (error bars are only shown for *a* and *c* for clarity); (B) temperature dependent variation of the unit cell volume. The dashed vertical line in both figures marks the magnetic ordering temperature at 17.8 K; lines fitted to the data are guides to the eye only.

coupling is antiferromagnetic. The magnetic space group is obtained as $P2_1/c'$. This model differs qualitatively from the previous one in $P\bar{1}$ [4], while extracted magnetic moments remain unchanged.

3.1.2.2. Possible Fe–Fe exchange paths. The topology of the $P2_1/c$ structure of $LiFeSi_2O_6$ allows different possible exchange interactions. The intra-chain exchange interaction *J* (Fig. 4) involves either the O1*A* or the O1*B* oxygen atom. With an identical short Fe–Fe distance of 3.173(12) Å at 1.4 K, the exchange interaction via the Fe–O1*A*–Fe path takes an angle of 97.7(5)°, while the one via the Fe–O1*B*–Fe path takes an angle of 99.1(5)°. Following the Goodenough–Kanamori rules, qualitatively, right angle geometry of *M*–O–*M* (with *M* = transition metal) should lead to a ferromagnetic coupling [32] as the AFM term is argued to vanish [32]. This qualitative and generally too simple approach was recently discussed in more detail by Grodzicki et al. [33]. Streltsov and Khomskii [18] stated that small FM contributions in rectangular *M*–O–*M* configurations are quickly outbalanced by stronger AFM exchanges when the *M*–O–*M* angle exceeds ~97° [18]. As we observe FM coupling within the *M*1 chain, Fe–Fe magnetic super-exchange may be favoured along the Fe–O1*A*–Fe path with the more rectangular configuration.

The interaction between two neighbouring *M*1 chains J_1 involves the SiO_4 tetrahedra. As two different tetrahedral chains are present in the $P2_1/c$ structure of $LiFeSi_2O_6$ one has to discern two different Fe–Fe coupling pathways. At 1.4 K the shortest distance between two neighbouring *M*1 chains is 5.280(12) Å and it involves the O1–O2 edge of the Si*B*-tetrahedron, while the shortest distance between *M*1 chains involving the Si*A*-tetrahedron is 5.357(13) Å. However, the effective super-exchange pathlength along Fe–O1*A*–O2*A*–Fe is 6.766(15) Å, the corresponding bond angles are 111.1(5)° and 153.7(7)°, respectively. Along the Fe–O1*B*–O2*B*–Fe path, the bond angles are distinctly different with 142.7(7)° and 121.1(6)°, respectively, while the effective super-exchange path is somewhat shorter with 6.601(14) Å. Jodlauk et al. [20] and Streltsov and Komskii [18] discuss an additional diagonal Fe–Fe coupling scheme J_2 involving two tetrahedra and causing magnetic frustration. In $LiFeSi_2O_6$ the next nearest Fe–Fe distances are 6.441(13) and 6.555(13) Å, however super-exchange along this Fe–Fe exchange pathways also involves only one tetrahedron. It remains to be clarified if the magnetic super-exchange between Fe-pairs in two different chains can go along the O1–O2 edge of the tetrahedron only, or must involves the complete SiO_4 tetrahedron to get the covalence, necessary for super-exchange, from Si–O bonds.

3.1.2.3. Temperature dependence of the nuclear structure. As changes in unit cell dimensions are associated with the magnetic ordering, electrostriction (magneto-elastic coupling) of secondary structural parameters are also to be expected. Discontinuities in individual bond lengths at the magnetic phase transition are visible especially for the *M*1 site; however, these changes are within two times the standard deviation in most cases. Most "pronounced" are the variation of the short Fe–O1*A* and Fe–O1*B* bonds which may be related to the Fe–Fe coupling within and between the *M*1 chains (Fig. 5A). The $[Fe–Fe]_{inter}$ distance within the *M*1 chain does not change in the entire temperature range as does the Fe–O1*B*–Fe bond angle, while the Fe–O1*A*–Fe angle, which is the smaller one, decreases with decreasing temperature below T_N by ~2°. This can be seen as an additional hint that Fe–Fe coupling within the *M*1 chain may go via O1*A* rather than O1*B*.

The two shortest Fe–Fe distances between distinct *M*1 chains also exhibit some discontinuous alterations at the magnetic phase transition (Fig. 5B), i.e. the $[Fe–Fe]_{inter}$ distance via the Si*B*-site becomes shortened while along the Si*A*-path the Fe–Fe coupling distance increases with decreasing temperature. Some discontinuous variations are also observable for the Fe–O1–O2–Fe angles, involved in super-exchange via the Si*B* tetrahedra, while the corresponding angles for the Si*A* linkage do not show as clear alterations, i.e. magnetic super-exchange via the Si*B*-tetrahedron might be postulated to be stronger.

Discontinuous alterations in bond lengths and angles at the magnetic phase transition are not restricted to the *M*1 sites, but also involve the tetrahedral sites. Though observable, these changes are not as clear as for the *M*1 site and are within two times the estimated standard deviation (except Si*A*–O1*A* and Si*B*–O1*B*). Furthermore, for the tetrahedral sites the individual bond lengths, derived from the neutron diffraction data, deviate from those expected for SiO_4 tetrahedra (by extrapolating from the 100 K single-crystal data [4]), i.e. the tetrahedra appear to be distinctly distorted. For example the Si*A*–O1*A* and Si*A*–O1*B* bond lengths are 1.692(15) and 1.552(17) Å at 52 K, while the corresponding single-crystal values at 100 K are 1.634(2) and 1.594(2) Å, respectively [4]. The data of this study suggest the Si*A*–O1*A* bond lengths to increase up to 1.74(2) Å close to the magnetic phase transition, which is a very high and unusual value for a Si–O bond. At low temperatures, this Si*A*–O1*A* bond reduces to a typical value of 1.63(2) Å, which is similar to the one at 100 K. High resolution neutron diffraction data would be necessary to

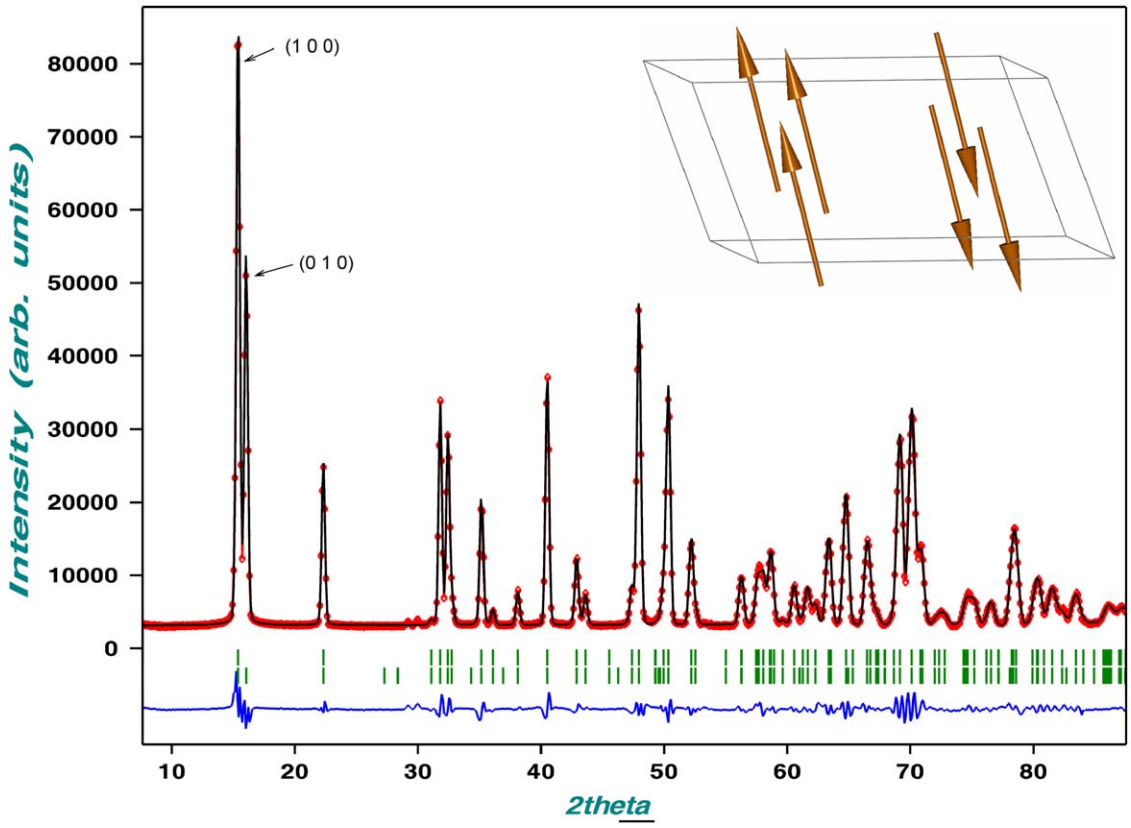

Fig. 3. Refined neutron diffraction pattern ($\lambda = 2.4249$ Å) of synthetic $LiFeSi_2O_6$ powder in the ordered state at 1.4 K with the corresponding spin arrangement plotted in the inset.

Table 3
Fe—positions at the 4*e* site in $LiFeSi_2O_6$ in space group $P2_1/c$ within one primitive unit cell.

Label (G_k)	Elem.	Symm. Op.	+ (*x*, *y*, *z*)	*x*	*y*	*z*
Fe_1	1	*x*, *y*, *z*	(0, 0, 0)	0.2455	0.6484	0.2386
Fe_2	2	$-x, y+\frac{1}{2}, -z+\frac{1}{2}$	(1, −1, 0)	0.7545	0.1484	0.2614
Fe_3	−1	−*x*, −*y*, −*z*	(1, 1, 1)	0.7545	0.3516	0.7614
Fe_4	*c*	$x, -y+\frac{1}{2}, z+\frac{1}{2}$	(0, 1, 0)	0.2455	0.8516	0.7386

Table 4
Possible magnetic structures based on basis vector analysis for $LiFeSi_2O_6$ in space group $P2_1/c$ and resulting magnetic space groups according to Litvin [30].

	Fe_1	Fe_2	Fe_3	Fe_4	Magn. S.G.
Γ_1	[***u***,***v***,***w***]	[−***u***,***v***,−***w***]	[−***u***,−***u***,−***w***]	[***u***,−***v***,***w***]	$\boldsymbol{P2_1/c'}$
Γ_2	[*u*,*v*,*w*]	[−*u*,*v*,−*w*]	[*u*,*v*,*w*]	[−*u*,*v*,−*w*]	$P2_1/c$
Γ_3	[*u*,*v*,*w*]	[*u*,−*v*,*w*]	[−*u*,−*v*,−*w*]	[−*u*,*v*,−*w*]	$P2_1'/c$
Γ_4	[*u*,*v*,*w*]	[*u*,−*v*,*w*]	[*u*,*v*,*w*]	[*u*,−*v*,*w*]	$P2_1'/c'$

clarify if such behaviour is an artefact of fitting. Concluding there are magneto-elastic effects in $LiFeSi_2O_6$ as probed by lattice parameters, their nature—being worth to be studied in some more detail—however cannot fully be described with the low resolution data available in this study.

3.2. $LiFeGe_2O_6$

3.2.1. Bulk magnetic properties

At an external field $H = 10$ kG the magnetic susceptibility χ_{molar} of synthetic $LiFeGe_2O_6$ exhibits a sharp maximum at 24.4(2) K in its temperature dependence with the point of inflection being located at 20.2(2) K (Fig. 6A). The inverse magnetic susceptibility $1/\chi_{molar}$ (inset of Fig. 6A) shows Curie–Weiss behaviour above ~100 K. Fitting a linear regression line to the data, the paramagnetic Curie-temperature was found to be negative with $\Theta_P = -78.6(5)$ K, the experimental magnetic moment $\mu_{CW} = 6.16(5)\,\mu_B$. The magnetisation data were corrected for the susceptibility of the ferromagnetic impurity (see below) before determining the aforementioned magnetic key data. The strongly negative paramagnetic Curie-temperature suggests antiferromagnetic coupling in $LiFeSi_2O_6$.

Above 2 kG the field dependence of the magnetisation in $LiFeGe_2O_6$ is linear (Fig. 6B), however a sluggish deviation from linearity takes place above ~25 kG for temperatures between 5 and 20 K. For higher temperatures the field dependency is strictly linear (except the very low fields). This behaviour evidences a spin rotation; most probably this is a spin-flip transition at external fields of 40–48 kG, depending on temperature. With the available data a *T*–*H* phase diagram for $LiFeGe_2O_6$ was constructed which is displayed as inset in Fig. 6B. This spin rotation takes place at lower fields and is more pronounced as compared to the silicate. At very low external fields, the magnetisation of $LiFeGe_2O_6$ exhibits the presence of a small ferromagnetic "impurity" in the sample, which was not detectable in the X-ray powder diffraction data. This "impurity" shows ferromagnetic behaviour up to room temperature with no hysteresis effects when switching the external field from positive to negative.

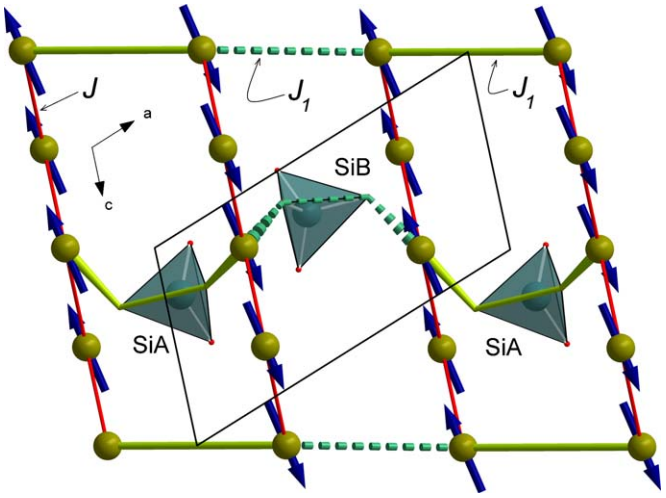

Fig. 4. Magnetic structure of synthetic $LiFeSi_2O_6$ viewed projected onto the *a*–*c* plane; Fe–Fe atoms are connected marking possible coupling paths: red = intra-chain coupling *J*, green = inter-chain coupling via the Si*A* tetrahedra, dashed sea-green line = inter-chain coupling via the Si*B* tetrahedra; the coupling scheme is also valid for $LiFeGe_2O_6$. (For interpretation of the references to colour in this figure legend, the reader is referred to the web version of this article.)

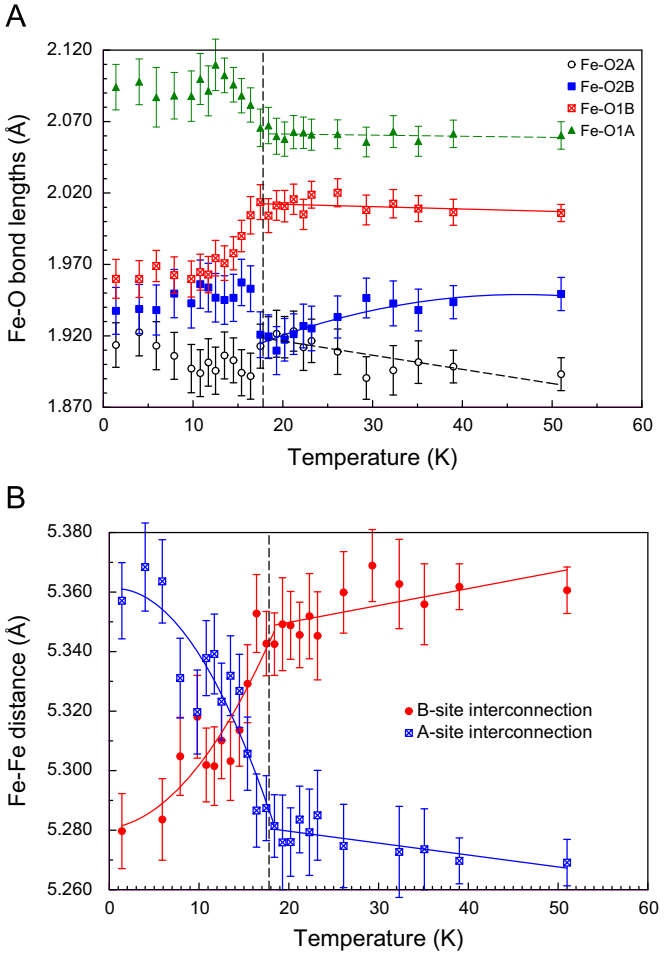

Fig. 5. (A) Changes in selected Fe–O bond-lengths at the *M*1 octahedron; (B) changes in the inter-chain Fe–Fe distances in $LiFeSi_2O_6$ through the magnetic phase transition. The dashed vertical line marks the magnetic ordering temperature, lines fitted to the data are guides to the eye only.

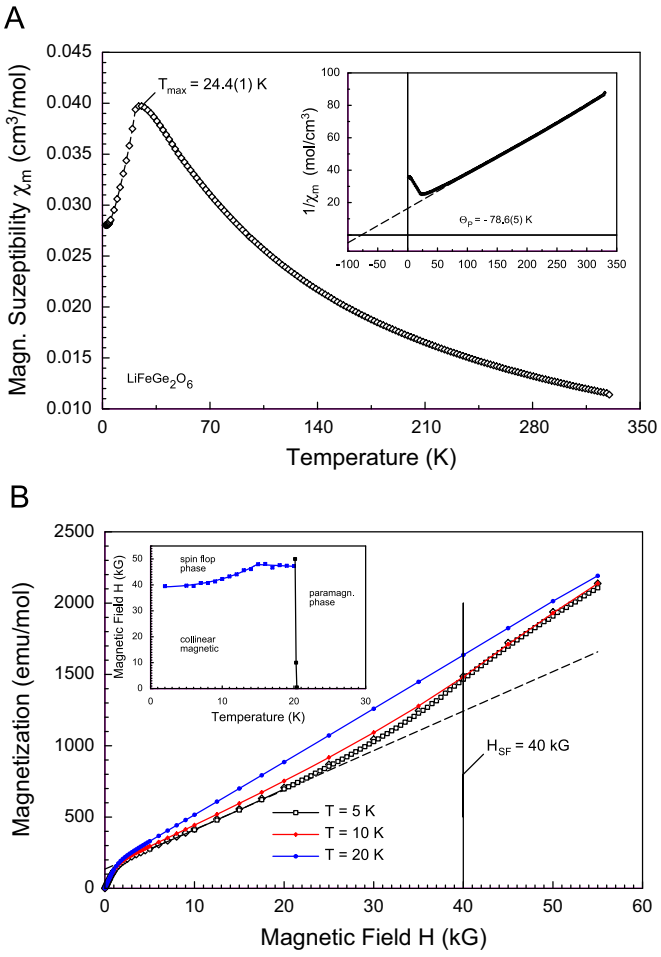

Fig. 6. (A) Magnetic susceptibility of synthetic $LiFeGe_2O_6$ at an external field of $H = 10$ kG. The inset shows the inverse magnetic susceptibility, the line fitted to the data corresponds to a Curie–Weiss law; (B) field dependence of $LiFeGe_2O_6$ at three selected temperatures. The long-dashed line is a linear regression line fitted to the low field (2.5–20 kG) data to highlight the upward deviation of the magnetisation at low temperatures. The very low field part marks the presence of a ferromagnetic impurity phase, which, however could not be quantified. The inset shows a *T*–*H* phase diagram, determined from the available data of this study.

3.2.2. *Neutron diffraction*

High resolution neutron diffraction data for $LiFeGe_2O_6$ were collected between 5 and 30 K. The atomic structure was refined using a 100 K structure of $LiFeGe_2O_6$ (single-crystal X-ray diffraction data; Redhammer, unpublished) as a starting model. With this, the 30 K data could satisfactorily be refined down to $R_{wp} = 4.77\%$ as depicted in Fig. 7. Experimental details and fitting parameters for selected temperatures are compiled in Table 1, while selected structural data are given in the Table 2.

3.2.2.1. Structure of $LiFeGe_2O_6$. $LiFeGe_2O_6$ shows $P2_1/c$ symmetry at 30 K and no evidence is observed for a symmetry change down to 5 K. The geometry of the atomic structure at 30 K is similar to $LiFeSi_2O_6$ with the main difference concerning the tetrahedral sites. Ge^{4+} in tetrahedral coordination has a distinctly larger ionic radius of 0.40 Å [34] as compared to Si^{4+} (0.26 Å; [34]) this increases the average Ge*A*–O distances by ~0.13 Å, the average Ge*B*–O bond length is larger by ~0.115 Å as compared to the corresponding Si–O bond lengths. Consequently also the tetrahedral O–O edges become enlarged. The O1*A*–O2*A* and O1*B*–O2*B* edges of the tetrahedra, involved in Fe–Fe coupling between *M*1

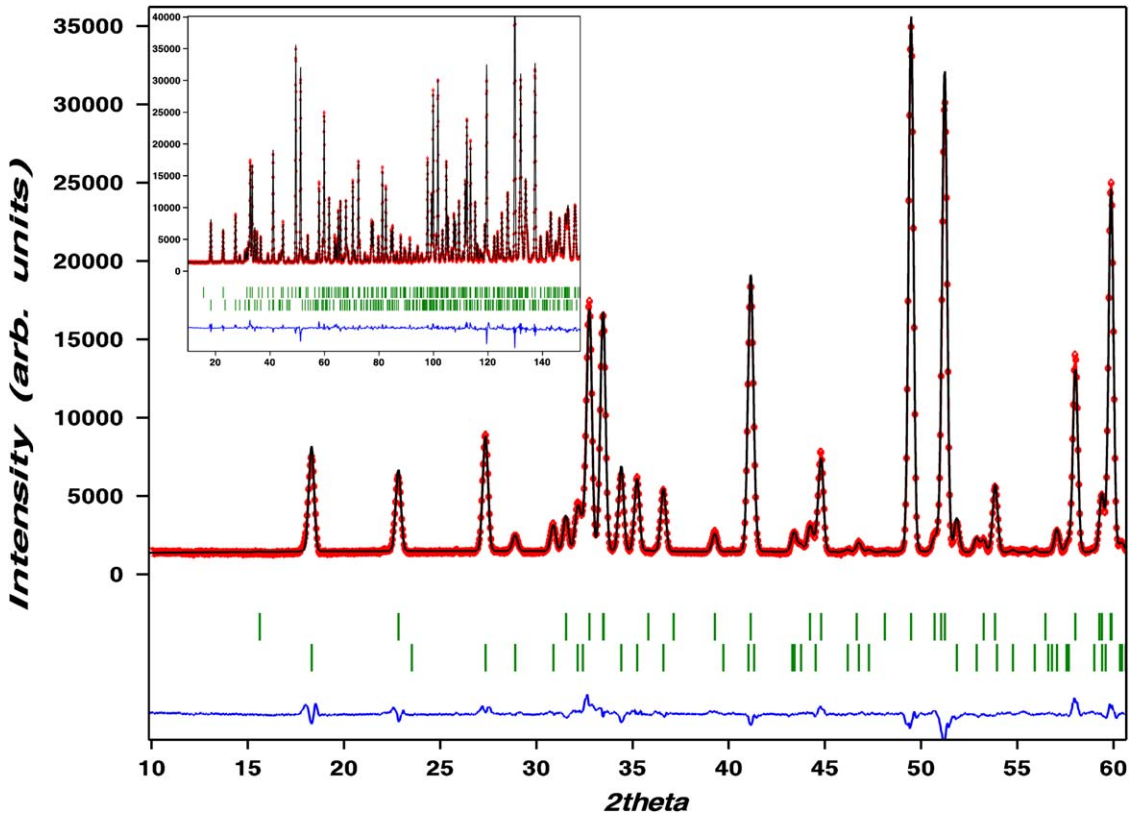

Fig. 7. Low angle part of the neutron diffraction pattern of $LiFeGe_2O_6$ ($\lambda = 2.537$ Å) collected at 5 K at the SPODI diffractometer, the inset shows the full pattern. The tick marks show the position of the nuclear (upper) and of the magnetic (lower) Bragg-peaks.

chains are longer by ~0.19 and 0.245 Å, respectively, in the germanate. The fit of the enlarged tetrahedral sites to the *M*1 chains is facilitated by an increased kinking state of the tetrahedral chains: in the *A*-chain, which is S-rotated in both compounds (bridging angle $>180^\circ$ [5]), the O3–O3–O3 tetrahedral bridging angle increases by almost 20° to ~209.5° while the *B*-chain, exhibiting an O-rotational sense, decreases its O3–O3–O3 kinking angle by more than 25° to 136.7°. The latter value is close to the limiting kinking state of 120° and is rarely observed in the clinopyroxenes.

Naturally the increased size of the tetrahedra moves the *M*1 chains further away from each other. Compared to the silicate, the difference between the two shortest Fe–Fe distances along the *A*- and the *B*-tetrahedral chain pathway is distinctly larger, as are the chain separations themselves. The $[Fe–Fe]_{inter}$ distance via the *A*-site tetrahedron is 5.420(2) Å and is ~0.09 Å longer than in the silicate, while the corresponding distance via the *B*-site tetrahedron is 5.544(2) Å being almost 0.25 Å longer than in the silicate. The angles of the Fe–O1*A*–O2*A*–Fe path are 107.3(2)° and 158.4(2)° at 5 K in the germanate, i.e. they are more different from each other than in the silicate (~111° and ~154°, respectively), while for the Fe–O1*B*–O2*B*–Fe path the two angles become more similar in the germanate with 135.4(2)° and 125.2(2)° as compared to ~143° and ~121° in the analogue silicate. The average Fe–O bond length is quite similar in $LiFeGe_2O_6$ and $LiFeSi_2O_6$, the distortion of the octahedra, however, changes, especially with respect to the [Fe–Fe] intra-chain coupling path. The Fe–Fe separation increases from 3.182(13) Å in the silicate to 3.215(2) Å in the germanate compound (both data at 20 K). While the two longer Fe–O1*A*, O1*B* bonds are quite similar, the shorter Fe–O1*A*, O1*B* bonds suffer distinct alterations: Fe–O1*A* becomes shorter, Fe–O1*B* larger by ~0.06 Å in $LiFeGe_2O_6$. The O1*A* and O1*B* oxygen atoms are corners of the octahedron and—at the same time—the apex atoms of the tetrahedra. Thus bonds to these O atoms naturally are very sensitive to the altered size requirements of the GeO_4 tetrahedra. As a consequence of this bond lengths alteration, the Fe–O1*A*–Fe angle increases from ~97.7° in $LiFeSi_2O_6$ to 101.6° in the germanate. This altered topology in $LiFeGe_2O_6$ with Fe–O–Fe bonding angles $>100^\circ$ may now favour antiferromagnetic super-exchange within the *M*1 chains.

The coordination of Li is strongly influenced by the conformational state of the GeO_4 tetrahedral chains. Due to the strong kinking of chains in $LiFeGe_2O_6$, the Li–O3*A* bond is shortened from 2.572(6) to 2.342(3) Å at 30 K, the Li–O3*B* bond decreases from 2.718(5) to 2.461(3) Å. This leads to a more uniform 6-fold coordination of the *M*2 site in $LiFeGe_2O_6$, which may be described by a distorted octahedron.

3.2.2.2. Magnetic structure of $LiFeGe_2O_6$. First additional Bragg reflections in the neutron diffraction data appear between 20 and 17 K. In contrast to $LiFeSi_2O_6$ the magnetic reflections cannot be indexed with $\boldsymbol{k} = 0$, but reveal a propagation vector of $\boldsymbol{k} = (\frac{1}{2}, 0, 0)$, i.e. a doubling of the *a*-lattice parameter is observed for the magnetic phase. Similar to $LiFeSi_2O_6$, the possible magnetic structures, compatible with the $P2_1/c$ symmetry of $LiFeGe_2O_6$, were determined by representational analysis. The possible magnetic structures for $LiFeGe_2O_6$ were again calculated with BasiReps [27] using the projection operation technique and are summarized in Table 5. Refinement of these possible magnetic structures against the 5 K data showed that the magnetic structure of $LiFeGe_2O_6$ can only be given by Γ_2 with the basis functions: $[C_x, A_y, C_z]$, and $R_{mag} = 10.0\%$. This corresponds to a magnetic structure with antiferromagnetically coupled spins

within the *M*1 chains (Fig. 8A). The appearance of AFM coupling within the *M*1 chains is consistent with large Fe–O–Fe angles $>100^\circ$ for both possible intra-chain exchange pathways in the germanate. The inter-chain coupling, however, is *different*, depending on the nature of the super-exchange pathway: $[Fe–Fe]_{inter}$ coupling via the Ge*A* tetrahedron is ferromagnetic. This is the shorter Fe–Fe distance between two neighbouring Fe-chains (5.420(2) Å at 5 K) with one small (107.2(3)°) and one large (158.3(3)°) Fe–O–O angle. Contrarily, the $[Fe–Fe]_{inter}$ coupling via the Ge*B* tetrahedron is antiferromagnetic. The Fe–O–O angles here are 125.2(3)° and 135.4(3)° with the Fe-atoms being separated by 5.544(2) Å at 5 K. The magnetic space group consistent with this ordering scheme is $P2_1'/c$ (Tables 5 and 6). Obviously, the distinct difference in Fe–Fe distances, Ge–O bond lengths and Fe–O–O–Fe angles, together with the higher covalence of Ge^{4+}, results in the alternating FM and AFM inter-chain coupling, which finally is the reason for the doubling of the magnetic unit cell along the *a*-axis. This inter-chain interaction however shows distinctly, that even for geometries far away from the rectangular case, the antiferromagnetic term in the magnetic coupling constant may vanish, yielding a FM coupling. Consequently the application of these "rules of the thumb" may be questioned, at least for super-exchange involving more than one atom. Theoretical calculations will be needed to get a more complete picture of the magnetic super-exchange coupling and for the electronic structure

Table 5
Bulk magnetic data from magnetisation measurements and components and resulting total magnetic moments in synthetic $LiFe(Ge,Si)_2O_6$ clinopyroxene compounds as extracted from Rietveld refinement on neutron diffraction data.

	$LiFeSi_2O_6$	$LiFeGe_2O_6$
Bulk magnetic data		
T_N (K) @ 10 kG	18.4(2)	20.2(2)
μ_{CW} (μ_B)	5.78	6.16
θ_P (K)	−25.4	−78.6
Neutron diffraction data		
Temperature (K)	1.4	5
M_x (μ_B)	0.52(8)	4.51(2)
M_y (μ_B)	0.05(6)	0.03(4)
M_z (μ_B)	4.83(5)	1.38(5)
M (μ_B)	4.85(5)	4.48(5)
$2\sqrt{S(S+1)}\mu_B$ [a]	5.92	5.92
$\angle(c, M)$ (°)	5.8(6)	91.0(5)
$\angle(a/c, M)$ (°)	–	–
J_{intra}	FM	AFM
J_{inter}	AFM	AFM, FM
Magn. space group	$P2_1/c'$	$P2_1'/c$

T_N = Neel temperature, μ_{CW} = experimental magnetic moment, θ_P = paramagnetic Curie temperature, determined from Curie–Weiss behaviour.

[a] Theoretical spin only value of the magnetic moment, $\angle(c, M)$ = angle between the magnetic moment and the crystallographic *c*-axis, $\angle(a/c, M)$ = angle between the magnetic moment and the crystallographic *a*–*c* plane.

Table 6
Possible magnetic structures based on basis vector analysis for $LiFeGe_2O_6$ in space group $P2_1/c$ and $k = (1/2, 0, 0)$ with resulting magnetic space groups according to Litvin [30], atom positions are the ones given in Table 3.

	Fe_1	Fe_2	Fe_3	Fe_4	Magn. S.G.
Γ_1	[*u*,*v*,*w*]	[*u*,−*v*,*w*]	[*u*,*v*,*w*]	[*u*,−*v*,*w*]	$P2_1'/c'$
$\boldsymbol{\Gamma_2}$	[***u***,***v***,***w***]	[***u***,−***v***,***w***]	[−***u***,−***v***,−***w***]	[−***u***,***v***,−***w***]	$\boldsymbol{P2_1'/c}$
Γ_3	[*u*,*v*,*w*]	[−*u*,*v*,−*w*]	[*u*,*v*,*w*]	[−*u*,*v*,−*w*]	$P2_1/c$
Γ_4	[*u*,*v*,*w*]	[−*u*,*v*,−*w*]	[−*u*,−*u*,−*w*]	[*u*,−*v*,*w*]	$P2_1/c'$

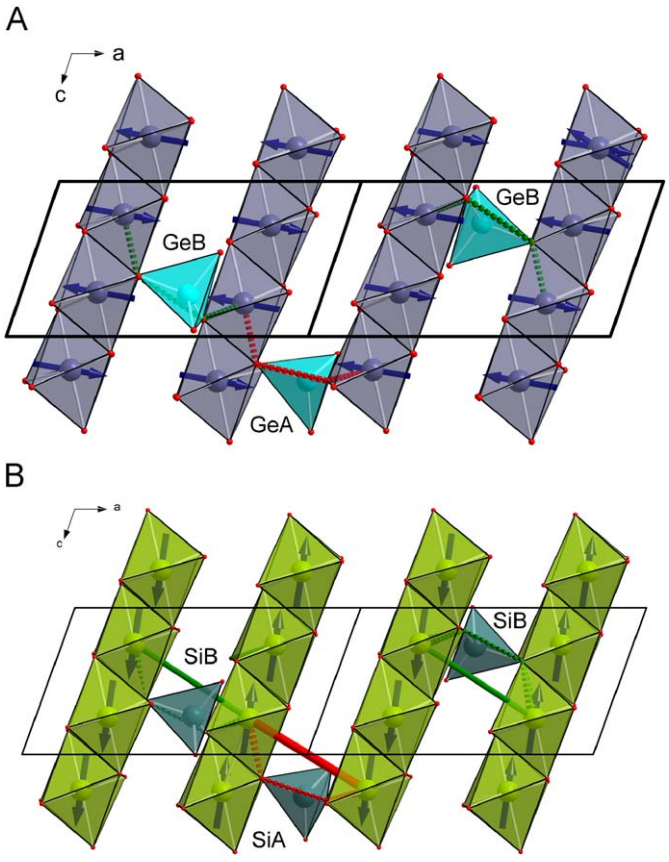

Fig. 8. (A) Magnetic structure of $LiFeGe_2O_6$ in a view onto the *a*–*c* plane showing $Fe^{3+}O_6$ *M*1 octahedral chains with spin orientation and exchange pathways between *M*1 chains via *A* and *B* tetrahedra. Li and most of the tetrahedral sites are omitted for clarity, the magnetic unit cell is doubled along the *a*-direction; (B) magnetic structure of $LiFeSi_2O_6$ in the same orientation, two magnetic cells are displayed along *a* for direct comparison.

necessities and interactions of *d*-orbitals with *p*-orbitals of the bridging ligand(s) behind this behaviour.

The magnetic spins are aligned within the *a*–*c* plane forming an angle of 91.0° with the *c*-axis. Still oriented within the *a*–*c* plane, the spins are rotated around *b* by nearly 90° when changing the tetrahedral cation from Si^{4+} to Ge^{4+} (Fig. 8A and B). The total magnetic moment at 5 K is 4.48(5) μ_B; this is a 24.3% reduction to the spin only value of high spin Fe^{3+} and also is a 8% reduction to the value found in the silicate. Finally it is interesting to note that the simple substitution of Si^{4+} by Ge^{4+} causes such distinct change in the magnetic structure of these isotypic clinopyroxenes.

3.2.2.3. Temperature dependence of the nuclear structure. The evolution of lattice parameters with temperature in $LiFeGe_2O_6$ is distinct from the silicate in two ways: (i) it does not display pronounced discontinuities at the magnetic phase transition and (ii) except *a*—all other lattice parameters decrease with increasing temperature. This latter behaviour however fits well the lattice parameters of $LiFeGe_2O_6$ determined from X-ray powder diffraction data between 25 and 1000 K (Redhammer, unpublished). In these data a positive lattice expansion coefficient is observed above 100 K. The negative thermal expansion at low temperatures may result from strong magneto-elastic coupling. Similar to the silicate, the *a* lattice parameter shows the smallest relative change in the entire temperature range, while *b* changes most (Fig. 9A).

Generally, hardly any anomalies in structural parameters can be observed when going through the magnetic phase transition.

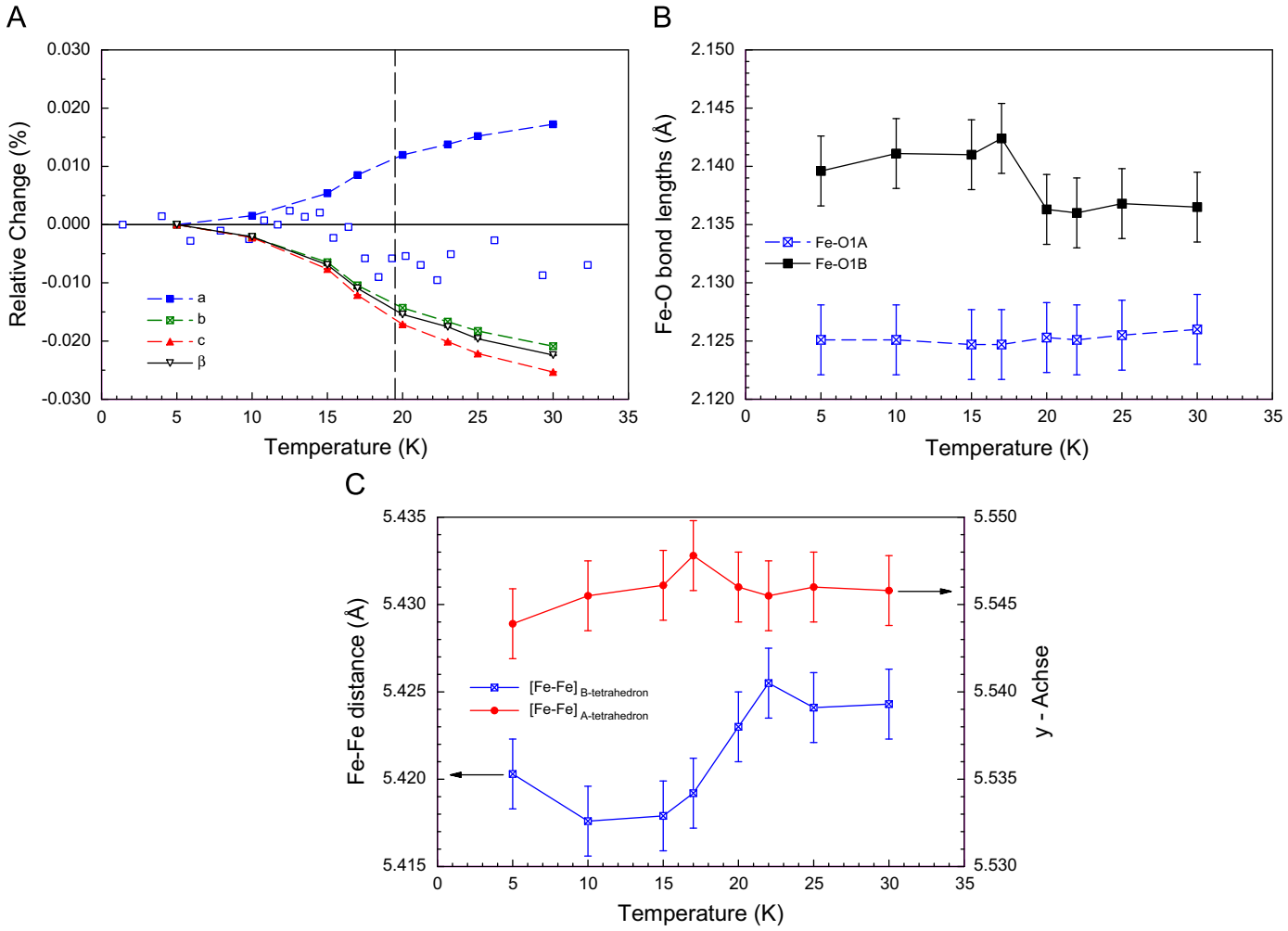

Fig. 9. (A) Relative changes in unit cell dimensions of $LiFeGe_2O_6$ with respect to the value at 5 K; open squares are data for the *a*-cell parameter of $LiFeSi_2O_6$ shown for comparison; (B) changes in Fe–O bond lengths with temperature in $LiFeGi_2O_6$ through the magnetic phase transition; (C) interatomic distances of Fe–Fe atoms between two different *M*1 chains.

Most "prominent" alterations are observed for the *M*1 site, changes are however within 2 standard deviations of the data. Only for the long Fe–O1*B* bond obvious changes are present, while the long Fe–O1*A* bond remains completely unaltered (Fig. 9B). The Fe–O1–Fe angles also remain constant within one estimated standard deviation with the exchange angle via the O1*B* oxygen atom becoming smaller by 0.3°, while the Fe–O1*A*–Fe angle slightly increases by 0.2°. From these observations it may be argued that super-exchange via the O1*B* oxygen (with the smaller Fe–O–Fe angle and small magnetostriction effects) is more favourable for Fe–Fe coupling. The Fe–Fe distance within the *M*1 chains is ~0.003 Å larger in the magnetically ordered phase, as compared to the paramagnetic phase; this was not observed for the FM coupled Fe-atoms within the *M*1 chains of $LiFeSi_2O_6$, even if magnetostriction is distinctly larger in the silicate. The Fe–Fe distances between the *M*1 chains show slightly different temperature behaviour (Fig. 9C); the Fe–Fe distance between chains with AFM coupling, i.e. those via the Ge*B* sites, become slightly more shortened upon the phase transition, as compared to the FM coupled *M*1 chains (*A*-site interconnection). AFM coupling of *M*1 chains, connected via the *B*-site tetrahedra, also causes a shortening of Fe–Fe distances in $LiFeSi_2O_6$, similar to the germanate compound.

Individual bond lengths of the GeO_4 tetrahedra show no clear discontinuities upon the phase transition. This distinctly contrasts the observations obtained for the silicate. Only for the Ge*A*–O1*A* and the Ge*B*–O1*B* distances some abnormal behaviour may be noted when passing trough the phase transition.

4. Conclusion

The clinopyroxene compounds $LiFeSi_2O_6$ and $LiFeGe_2O_6$ are isostructural and the nuclear structure displays $P2_1/c$ symmetry down to low temperatures of 1.4 and 5 K, respectively. However, both compounds transform to a three-dimensional magnetically ordered state below $T = 20$ K. $LiFeSi_2O_6$ shows a quite simple magnetic structure with no indications of an incommensurate modulation. The magnetic space group is $P2_1/c'$ and the structure is described by a FM coupling within and an AFM coupling of spins between the *M*1 chains (Fig. 8B). The substitution of Ge^{4+} for Si^{4+} mainly increases the Fe–Fe separation within and between the *M*1 chains and also alters the Fe–O–Fe bonding geometry, important for super-exchange within the *M*1 chains. While in $LiFeSi_2O_6$ a Fe–O1*A*–Fe angle of ~97.7° allows FM coupling via the O1*A* oxygen atom (by compensation of the AFM part to the coupling constant), this angle increases to ~101.6° in the germanate, then shows AFM coupling of spins within the *M*1 chains. A feature of the magnetic structure of $LiFeGe_2O_6$ is the appearance of a FM

coupling between the *M*1 chains, connected via the edge of the Ge*A* tetrahedron, while the *M*1 chains, connected via the edge of the Ge*B* tetrahedron are AFM coupled. This finally is the reason for the doubling of the magnetic cell along the *a*-axis, but no indication for an incommensurate modulation was found. The magnetic space group for $LiFeGe_2O_6$ is $P2_1'/c$. The very same magnetic space group was found recently for $LiCrSi_2O_6$ [35]. This clinopyroxene shows a commensurate ordering with $k = (0, 0, 0)$ and antiferromagnetic ordering of spins within the chains of CrO_6 octahedra, while the chain-to-chain ordering is ferromagnetic [35].

Though the germanate shows larger Fe–Fe distances within and between the *M*1 chains, $LiFeGe_2O_6$ has the higher magnetic ordering temperature. This higher ordering temperature can be related to the higher covalence of Ge^{4+} (as compared to Si^{4+}) and hints that the Ge^{4+} cation plays an important role in magnetic super-exchange between two different *M*1 chains. Consequently super-exchange may not only go along the edge of the TO_4 tetrahedra (i.e. pure dipole–dipole interactions) but includes the covalent *T*-cations also.

$LiFeGe_2O_6$ has a more negative paramagnetic Curie-temperature. This indicates that the AFM coupling within and between the *M*1 chains is strong and dominates over the FM coupling between *M*1 chains, coupled via the Ge*A* sites. On the other hand the negative paramagnetic Curie-temperature on $LiFeSi_2O_6$ indicates that J_1 (coupling between the chains) dominates J (in-chain coupling).

The magnetic structure of $LiFeGe_2O_6$ exhibits a ferromagnetic coupling of spins between *M*1 chains (coupled via $GeAO_4$), even if the bonding geometry is far away from a rectangular geometry. This shows that—at least in the present case—phenomenological, geometric rules such as the Goodenough–Kanamori rules should not be applied to exchange interactions involving more than one atom. Further it is evident from the results above, that for a better understanding of the magnetic and multiferroic behaviour in pyroxenes theoretical, quantum-chemical calculations are needed. As is shown by $LiFeSi_2O_6$, the temperature dependent changes of the nuclear structure can be large and discontinuous. In theoretical studies an extrapolation of structural data from room temperature to low temperature thus cannot reflect actual properties and reliable low temperature structural data must be used instead. It was one aim of this study to provide such reliable data on nuclear and magnetic structure at very low temperatures.

Acknowledgement

We acknowledge the help of H. Ehrenberg (Dresden) in performing the high field magnetic susceptibility measurements on $LiFeSi_2O_6$. This work was supported by the Austrian "Fonds zur Förderung der wissenschaftlichen Forschung (FWF)" under Grant P19762-N10.

Appendix A. Supplementary material

Supplementary data associated with this article can be found in the online version at 10.1016/j.jssc.2009.06.013.

References

[1] M. Cameron, J.J. Papike, Am. Mineral. 66 (1981) 1–50.
[2] G.J. Redhammer, G. Roth, Z. Kristallogr. 219 (2004) 278–294.
[3] R.M. Thompson, R.T. Downs, G.J. Redhammer, Am. Mineral. 90 (2005) 1840–1851.
[4] G.J. Redhammer, G. Roth, W. Paulus, G. André, W. Lottermoser, G. Amthauer, W. Treutmann, B. KoppelhuberBitschnau, Phys. Chem. Miner. (2001) 337–346.
[5] G.J. Redhammer, G. Roth, Z. Kristallogr. 219 (2004) 585–605.
[6] T. Arlt, R.J. Angel, Phys. Chem. Miner. 27 (2000) 719–731.
[7] T. Arlt, R.J. Angel, R. Miletich, T. Armbruster, T. Peters, Am. Mineral. 83 (1998) 1176–1181.
[8] F. Nestola, T. Boffa Balleran, H. Ohashi, Phys. Chem. Miner. 35 (2008) 477–484.
[9] M. Isobe, E. Nimomiya, A.N. Vasil'ev, Y. Ueda, J. Phys. Soc. Jpn. 71 (6) (2002) 1423–1426.
[10] G.J. Redhammer, H. Ohashi, G. Roth, Acta Crystallogr. B 59 (2003) 730–746.
[11] J.L. Gavilano, S. Mushkolaj, H.R. Ott, P. Millet, F. Mila, Phys. Rev. Lett. 85 (2) (2000) 409–412.
[12] M.D. Lumdsen, G.E. Granroth, D. Mandrus, S.E. Nagler, J.R. Thoompson, J.P. Castellan, B.D. Gaulin, Phys. Rev. B 63 (14) (2000) R9244–R9247.
[13] P. Vonlanthen, L.B. Tanaka, A. Goto, Phys. Rev. B 65 (21) (2002) Art.Nr. 214413.
[14] M. Isobe, Y. Ueda, A.N. Vasiliev, T.N. Voloshok, O.L. Ignatchik, J. Magn. Magn. Mater. 256 (2003) 125–127.
[15] B. Pedrini, S. Wessel, J.L. Gavilano, H.R. Ott, S.M. Kazakov, J. Karpinski, Eur. Phys. J. B 55 (2007) 219–228.
[16] A.N. Valiliev, A.N. Ignatchik, A.N. Sokolov, Z. Hiroi, M. Isobe, Y. Ueda, JEPT Lett. 78 (9) (2003) 551–554.
[17] A.N. Valiliev, A.N. Ignatchik, A.N. Sokolov, Z. Hiroi, M. Isobe, Y. Ueda, Phys. Rev. B 72 (2005) 012412 (4pp).
[18] S.V. Streltsov, D.I. Khomskii, Phys. Rev. B 77 (2008) 064405 (11pp).
[19] G.J. Redhammer, G. Roth, G. Amthauer, Acta Crystallogr. C 64 (2008) i97–i102.
[20] S. Jodlauk, P. Becker, J.A. Mydosh, D.I. Khomskii, T. Lorenz, S.V. Streltsov, D.C. Hezel, L. Bohaty, J. Phys. Condens. Matt. 19 (2007) 432201 (9pp).
[21] G.J. Redhammer, G. Roth, W. Treutmann, W. Paulus, G. André, C. Pietzonka, G. Amthauer, J. Solid State Chem. 181 (2008) 3163–3176.
[22] J. Rodrigues-Carvajal, CPD Newsl. 26 (2001) 12–19.
[23] G. Cagliotti, A. Paoletti, F.P. Ricci, Nucl. Instr. 3 (1958) 223–228.
[24] H. Lueken, Magnetochemie, Teubner Studienbücher, Stuttgart-Leipzig, 1999 (in German).
[25] E. Baum, W. Treutmann, M. Behruzi, W. Lottermoser, G. Amthauer, Z. Kristallogr. 183 (1988) 273–284.
[26] K. Hagdorn, D. Hohlwein, J. Ihringer, K. Knorr, W. Prandl, H. Ritter, H. Schmid, T. Zeiske, Eur. Phys. J. Condens. Matt. B 11 (1999) 243–254.
[27] E.F. Bertaut, Acta Crystallogr. A 24 (1968) 217.
[28] E.F. Bertaut, in: G.T. Rado, H. Suhl (Eds.), Magnetism, vol. III, 1963, pp. 149–209 (Chapter 4).
[29] J. Rodriquez-Charvajal, BasiReps: A program for calculating irreducible representation of little groups and basis functions of polar and axial vector properties, 2004.
[30] D.B. Litvin, Acta Crystallogr. A 64 (2008) 419–424.
[31] S.J. Blundell, C.A. Steer, F.L. Pratt, I.M. Marshall, W. Hayes, R.C.C. Ward, Phys. Rev. B 67 (2003) 224411.
[32] J.B. Goodenough, Magnetism and the Chemical Bond, Interscience, New York, 1963.
[33] G. Grodzicki, G.J. Redhammer, M. Reissner, W. Steiner, G. Amthauer, Am. Mineral. 2009, Phys. Chem. Minerals, doi: 10.1007/s00269-009-0306-2, in press.
[34] R.D. Shannon, C.T. Prewitt, Acta Crystallogr. B 25 (1969) 925–946.
[35] G. Nenert, M. Isobe, C. Ritter, O. Isnard, A.N. Vasiliev, Y. Ueda, Phys. Rev. B 79 (2009) 064416 (8pp).